

# MuxGel: Simultaneous Dual-Modal Visuo-Tactile Sensing via Spatially Multiplexing and Deep Reconstruction

Zhixian Hu, Zhengtong Xu, Sheeraz Athar, Juan Wachs, Yu She

**Abstract**—High-fidelity visuo-tactile sensing is important for precise robotic manipulation. However, most vision-based tactile sensors face a fundamental trade-off: opaque coatings enable tactile sensing but block pre-contact vision. To address this, we propose MuxGel, a spatially multiplexed sensor that captures both external visual information and contact-induced tactile signals through a single camera. By using a checkerboard coating pattern, MuxGel interleaves tactile-sensitive regions with transparent windows for external vision. This design maintains standard form factors, allowing for plug-and-play integration into GelSight-style sensors by simply replacing the gel pad. To recover full-resolution vision and tactile signals from the multiplexed inputs, we develop a U-Net-based reconstruction framework. Leveraging a sim-to-real pipeline, our model effectively decouples and restores high-fidelity tactile and visual fields simultaneously. Experiments on unseen objects demonstrate the framework’s generalization and accuracy. Furthermore, we demonstrate MuxGel’s utility in grasping tasks, where dual-modality feedback facilitates both pre-contact alignment and post-contact interaction. Results show that MuxGel enhances the perceptual capabilities of existing vision-based tactile sensors while maintaining compatibility with their hardware stacks. Project webpage: <https://zhixianhu.github.io/muxgel/>.

## I. INTRODUCTION

Effective robotic manipulation requires the integration of vision and touch [1]–[3]. Vision provides global context for planning and approach phases, whereas tactile sensing provides local feedback for contact detection [4], force regulation [5], and fine manipulation [6]. Traditionally, visual feedback is obtained through external or eye-in-hand cameras [7], [8]. However, as the end-effector approaches an object, these systems often encounter severe occlusion caused by the manipulator or the object. This limitation renders them unable to reliably observe the contact interface, necessitating a transition from global visual guidance to local tactile perception at the moment of interaction.

To capture detailed local information, tactile sensors are increasingly embedded directly into robotic fingertips [9]. Among various modalities, vision-based tactile sensors have gained prominence due to their high spatial resolution, compact mechanical design, and simple wiring. Several designs have addressed these requirements. GelSight utilizes RGB lighting and photometric stereo to reconstruct surface geometry [10]. TacTip tracks the displacement of internal structural

This material is partially based upon work supported by the National Science Foundation under Grant NSF #2140612 and NSF #2423068. Any opinions, findings, and conclusions or recommendations expressed in this material are those of the author(s) and do not necessarily reflect the views of the funding agencies.

Edwardson School of Industrial Engineering, Purdue University, West Lafayette, IN, USA. {jpwachs, shey}@purdue.edu

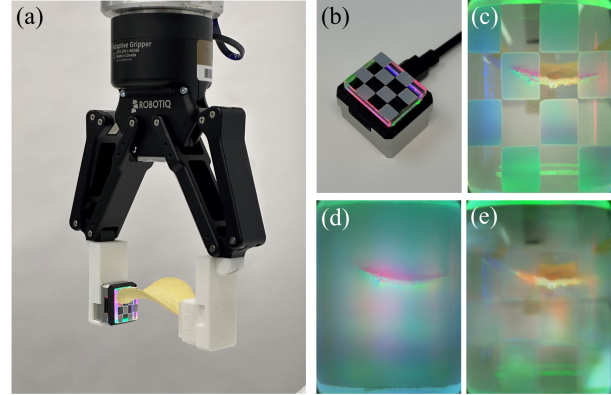


Fig. 1. Grasping a chip with MuxGel: (a) A Robotiq gripper grasping a chip using MuxGel for simultaneous visuo-tactile sensing via spatial multiplexing. (b) MuxGel with the 4x4 checkerboard configuration integrated into a GelSight Mini by replacing only the gel pad, without optical or mechanical redesign. (c) Raw multiplexed sensor output. (d) Reconstructed tactile image. (e) Reconstructed visual appearance image.

pins [11]. DelTact employs optical flow to estimate the deformation of dense color patterns [12]. DTact measures contact via semi-transparent and absorptive layers [13]. While these sensors excel in tactile perception, they are typically limited to a single tactile modality. Because these sensors rely on opaque internal coatings to capture deformation, they are unable to perceive the external environment and can only detect physical contact.

To bridge the occlusion gap and achieve simultaneous visuo-tactile perception, several dual-modal approaches have been proposed, though they often introduce new trade-offs. Adding a dedicated camera alongside a tactile sensor increases the fingertip size and introduces parallax, complicating cross-modal alignment [14], [15]. Alternatively, utilizing transparent elastomers with embedded visual markers reduces bulk [16]–[19], but the sparse distribution of these markers yields limited tactile spatial resolution and may compromise the capture of fine texture cues. Other research has explored mode-switching designs. While mechanical solutions like rolling switch modules [20] increase system complexity, material-driven approaches use special coatings or gels that alter transparency under different conditions to avoid hardware complexity [21]–[24]. However, because these sensors alternate between pre-contact vision and in-contact tactile sensing, they inevitably lose visual information during the critical contact phase, limiting continuous perception across the entire manipulation cycle.

To address these limitations, we introduce MuxGel, an

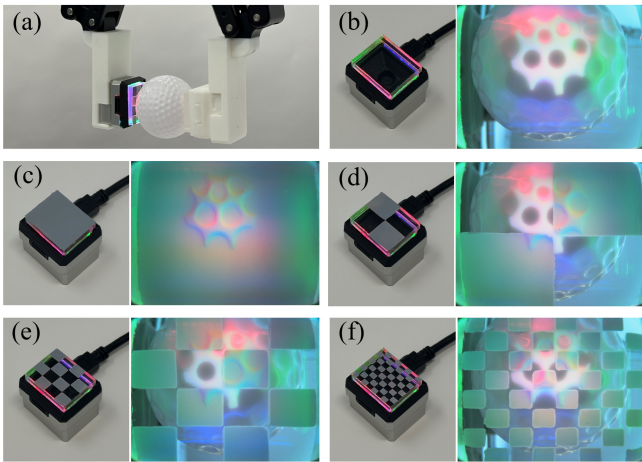


Fig. 2. MuxGel configurations and raw observations. (a) A 4x4 sensor integrated with a Robotiq gripper during a grasp. (b)-(f) Hardware patches (left) and captured images (right) for pure vision, pure tactile, and multiplexed (2x2, 4x4, 8x8) configurations.

integrated hardware and software framework that enables simultaneous high-resolution visuo-tactile perception via spatial multiplexing, as shown in Fig. 1. At the hardware level, MuxGel features a spatially multiplexed coating strategy, implemented as a checkerboard pattern, that dedicates distinct regions to visual appearance sensing and contact deformation. This design preserves the pad geometry and mechanical interface of standard GelSight-Style gel pads, enabling integration by replacing only the gel pad and requiring no optical or mechanical redesign. To effectively process this multimodal data, drawing on computational vision and image inpainting techniques [25]–[27], we propose a deep reconstruction pipeline using a shared ResNet encoder [28] with two U-Net-style decoders [29] to generate tactile and visual images. We further adopt a sim-to-real training strategy with large-scale physics-based simulation pre-training followed by real-world fine-tuning. Finally, we demonstrate the system’s generalization capabilities on unseen objects and validate its performance in robotic manipulation tasks, proving its capability to provide continuous real-time dual-modal feedback for robot manipulation.

## II. METHOD

### A. Hardware Design

The MuxGel sensor’s capabilities stem from a spatially multiplexed coating strategy. We follow the standard GelSight gel pad fabrication process, with a modified coating step. Specifically, instead of applying a uniform coating layer, we utilize a checkerboard-pattern mold to selectively apply gray Lambertian paint, yielding alternating coated and transparent regions. To evaluate the impact of coating resolution, we fabricated three checkerboard configurations ( $2 \times 2$ ,  $4 \times 4$ , and  $8 \times 8$ ), as shown in Fig. 2. To provide modality-specific ground truth, we also produced two baseline pads: a fully coated (tactile-only) pad and a transparent (vision-only) pad. This modular design allows for rapid pad exchange without changes to the underlying sensor hardware.

### B. Simulation Data Generation Pipeline

To reduce the cost of real-world data collection, we develop a randomized physics-based simulation pipeline. The pipeline synthesizes realistic spatially multiplexed images ( $\tilde{I}_{\text{mux}}$ ) by simulating the physical deformation, optical properties, and the MuxGel masking process, as shown in Fig. 3. The tilde notation ( $\tilde{\cdot}$ ) denotes synthetic data generated by our simulation pipeline, distinguishing it from real sensor data.

The Google Scanned Objects dataset was selected to populate the simulation environment, as it provides over 1000 high-fidelity 3D-scanned household items [30]. The environment is built in the MuJoCo physics engine [31] using the corresponding models [32]. A virtual camera is placed at 14 mm from the object surface to match the GelSight Mini geometry. For each object, we sampled 50 viewpoints to render RGB images ( $\tilde{V}_{\text{obj}}$ ) and depth maps ( $\tilde{D}$ ).

Tactile interaction is simulated by combining the rendered depth map with Taxim [33], which is optimized for GelSight Mini and exhibits low pixel-wise intensity errors. The depth map  $\tilde{D}$  is converted into an object height map and compared with the calibrated elastomer spatial profile to approximate soft deformation. Given a randomly sampled pressing depth ranging in  $[0.01, 1.5]$  mm, the intersection produces a contact mask ( $\tilde{M}_c$ ) and a relative contact height field. Following Taxim, surface gradients are mapped to illumination intensities via a calibrated polynomial table. Furthermore, to improve realism, a shadow generation algorithm employs ray-tracing approximations to cast shadows based on the contact geometry, outputting a raw tactile image ( $\tilde{T}_{\text{raw}}$ ).

To narrow the sim-to-real gap, we apply domain randomization that targets the sensor’s optics and shared illumination structure. In vision-based tactile sensing, the external scene is typically out of focus due to a narrow depth of field. Backgrounds ( $\tilde{V}_{\text{bg}}$ ) from the IndoorCVPR dataset [34] are integrated using a disk defocus blur. This blurred background is fused with  $\tilde{V}_{\text{obj}}$  using a background mask ( $\tilde{M}_{\text{bg}}$ ) derived from the depth and image intensity. The combined raw vision image  $\tilde{V}_{\text{raw}}$  is formulated as:

$$\tilde{V}_{\text{raw}} = \tilde{M}_{\text{bg}} \odot \tilde{V}_{\text{bg}} + (1 - \tilde{M}_{\text{bg}}) \odot \tilde{V}_{\text{obj}}, \quad (1)$$

To evaluate the decoupling network’s ability to handle complex real-world sensor noises, our pipeline supports two tactile target formulations: absolute and residual. In the absolute formulation, the raw simulated tactile image  $\tilde{T}_{\text{raw}}$  is utilized directly. In the residual formulation, we isolate the deformation-induced difference image  $\tilde{T}_{\text{diff}}$  by subtracting the no-contact tactile background

$$\tilde{T}_{\text{diff}} = \tilde{T}_{\text{raw}} - \tilde{T}_{\text{org,bg}}, \quad (2)$$

where  $\tilde{T}_{\text{org,bg}}$  is the simulated non-contact tactile background.

Because external ambient light leakage affects both modalities simultaneously, we apply correlated color jittering. In the absolute formulation, brightness, contrast, saturation, and hue are perturbed jointly for  $\tilde{T}_{\text{raw}}$  and  $\tilde{V}_{\text{raw}}$  to obtain  $\tilde{T}_{\text{jit}}$  and  $\tilde{V}_{\text{jit}}$ . In the residual formulation, this joint perturbation is applied to a randomly sampled real tactile background  $T_{\text{bg}}$

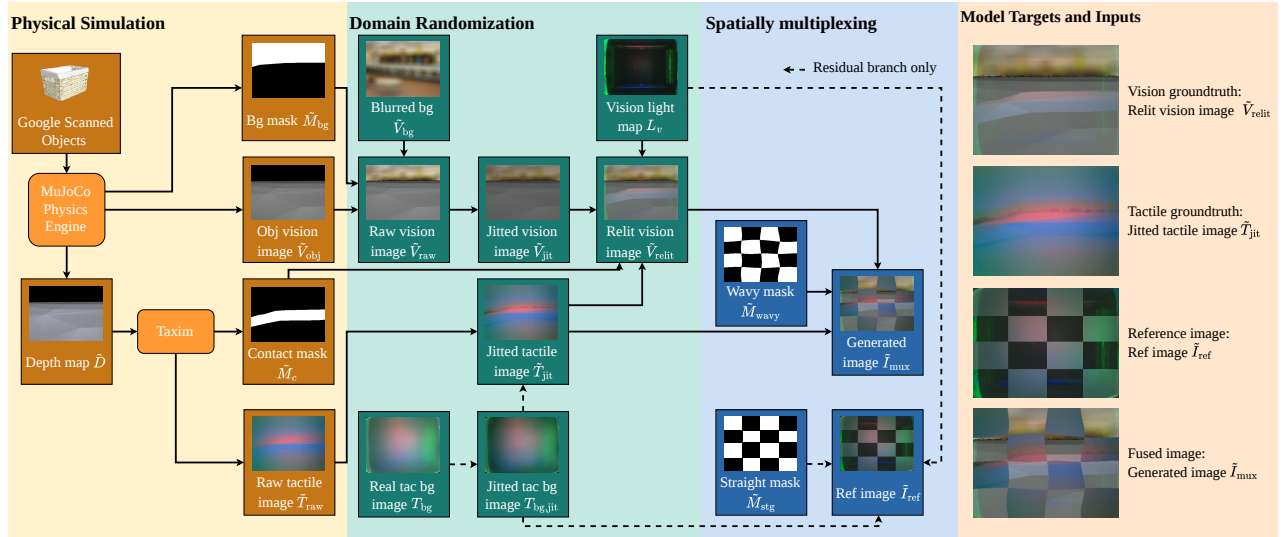


Fig. 3. Large-scale physics-based simulation pipeline for visual-tactile data generation. Bg: Background; Obj: Object; Tac: Tactile; Ref: Reference.

and  $\tilde{V}_{\text{raw}}$ , yielding  $T_{\text{bg,jit}}$  and  $\tilde{T}_{\text{jit}}$ , respectively. The final tactile image  $\tilde{T}_{\text{jit}}$  used for residual learning is then constructed as

$$\tilde{T}_{\text{jit}} = \tilde{T}_{\text{diff}} + T_{\text{bg,jit}}. \quad (3)$$

This correlated jittering mechanism encourages the network to learn fundamental structural differences rather than relying on trivial color shifts.

Moreover, the visual and tactile modalities in MuxGel share an internal optical environment. To simulate this, we utilize real blank sensor images captured in a dark environment as pure vision light maps ( $L_v$ ), and the processed tactile images ( $\tilde{T}_{\text{jit}}$ ) as the contact-induced tactile illumination field. We relight the jittered vision image by applying these priors in contact and non-contact regions, guided by the contact mask  $\tilde{M}_c$ :

$$\tilde{V}_{\text{relit}} = \tilde{M}_c \odot (\tilde{V}_{\text{jit}} \odot \tilde{T}_{\text{jit}}) + (1 - \tilde{M}_c) \odot (\tilde{V}_{\text{jit}} \odot L_v), \quad (4)$$

where  $\tilde{V}_{\text{relit}}$  denotes the relit vision image.

The final sensor observation is synthesized by applying a checkerboard mask. Instead of utilizing a perfect geometric pattern, we generate a random wavy checkerboard mask ( $\tilde{M}_{\text{wavy}}$ ) with base grids ranging from 2x2 to 8x8 grids to simulate manufacturing tolerances, elastomer warping, and lens distortions. The boundaries of the wavy mask  $B(t)$  are perturbed by:

$$B(t) = P_{\text{base}} + A \cdot \sin(2\pi ft + \phi), \quad (5)$$

where  $P_{\text{base}}$  is the nominal boundary position,  $A \in [0, 5.0]$  is a randomized amplitude,  $f$  is the spatial frequency, and  $\phi$  is a phase shift. The spatially multiplexed input  $\tilde{I}_{\text{mux}}$  to the network is then

$$\tilde{I}_{\text{mux}} = \tilde{M}_{\text{wavy}} \odot \tilde{T}_{\text{jit}} + (1 - \tilde{M}_{\text{wavy}}) \odot \tilde{V}_{\text{relit}}. \quad (6)$$

To facilitate the decoupling process, particularly for the residual learning formulation, our network requires a spatial reference image ( $\tilde{I}_{\text{ref}}$ ). This reference image is constructed

using a nominal straight checkerboard mask ( $\tilde{M}_{\text{stg}}$ ) corresponding to the base grid dimensions. The reference image  $\tilde{I}_{\text{ref}}$  acts as an illumination prior and an ideal multiplexing layout by compositing  $T_{\text{bg,jit}}$  and  $L_v$ :

$$\tilde{I}_{\text{ref}} = \tilde{M}_{\text{stg}} \odot T_{\text{bg,jit}} + (1 - \tilde{M}_{\text{stg}}) \odot L_v. \quad (7)$$

We concatenate  $\tilde{I}_{\text{mux}}$  and  $\tilde{I}_{\text{ref}}$  along the channel dimension, providing the model with a baseline optical distribution and the ideal multiplexing layout, thereby significantly mitigating the ill-posed nature of the separation task.

Finally, to ensure meaningful physical interaction, we filter samples by requiring the contact-area ratio in  $\tilde{M}_c$  to exceed 5%. Due to large variation in object geometry and scale, some scanned models fail to produce 50 valid patches after resampling and are discarded. The final dataset contains 848 objects with 50 viewpoints each. For every valid patch, we simulate five press depths, yielding a base set of 212,000 unique geometric contact profiles. Crucially, rather than utilizing a static dataset, the training samples are synthesized on-the-fly during each iteration. By dynamically applying the randomized wavy masks ( $\tilde{M}_{\text{wavy}}$ ), correlated color jittering, and random background selection ( $\tilde{V}_{\text{bg}}$ ), the effective training dataset becomes virtually infinite. This dynamic domain randomization strategy encourages the network to learn generalizable decoupling priors rather than memorizing a fixed set of synthetic samples.

### C. Reconstruction Framework

Following the generation of simulated fused data, we propose muxNet, a dual-stream reconstruction network designed to decouple entangled visual and tactile signals. To reduce the sim-to-real gap, muxNet is trained in two stages: large-scale pre-training on simulation data and fine-tuning on real data with physics-based augmentations. As shown in Fig. 4, muxNet adopts a modified ResNet34-UNet with a shared encoder and two task-specific decoders.

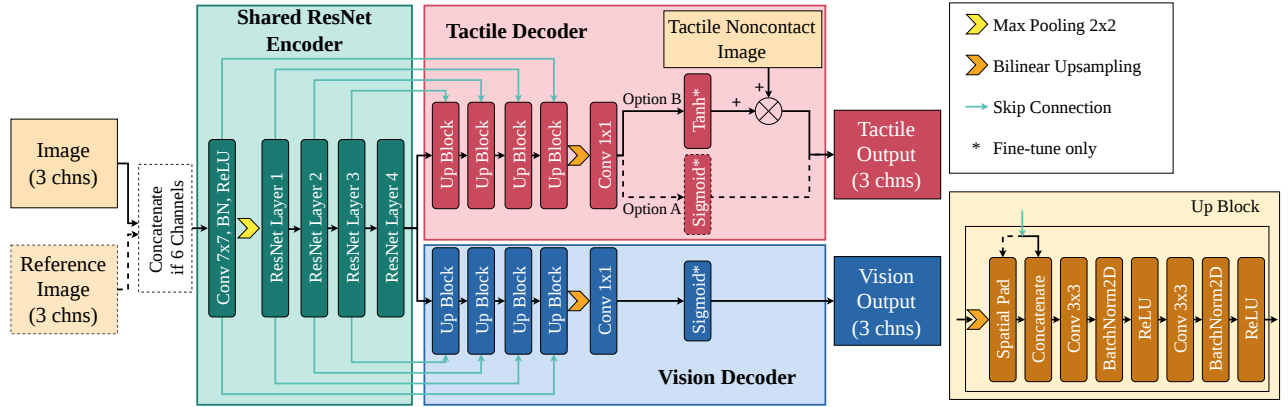


Fig. 4. Overview of the dual-stream muxNet architecture. A shared ResNet-34 encoder processes either a 3-channel fused image or a 6-channel tensor formed by concatenating the multiplexed image with a non-contact reference image. Two task-specific decoders reconstruct the visual and tactile modalities, respectively. The tactile branch supports absolute prediction (Option A) and residual prediction (Option B), where the predicted contact residual is added to the non-contact tactile image. Asterisks (\*) denote activation functions specific to real-data fine-tuning. Chns: channels. BN: BatchNorm. Conv: Convolution.

The network takes a 6-channel input formed by concatenating the current fused image and a non-contact reference image. A ResNet-34 backbone pre-trained on ImageNet is used as the shared encoder. The first convolution is adapted to accept 6 channels while preserving the pre-trained weights. During real-data fine-tuning, the encoder stem (initial convolution, normalization, and pooling) is frozen to stabilize low-level feature extraction and reduce catastrophic forgetting.

The model branches into two symmetric decoder streams with UNet-style upsampling and skip connections. The vision decoder reconstructs the visual RGB image. The tactile decoder is formulated as residual reconstruction. It predicts a tactile difference map that captures contact-induced deformations, and the final tactile image is obtained by adding the predicted residual to the non-contact tactile background. The final activation functions are applied only during real-data fine-tuning to bound the output ranges: Tanh is used for tactile residuals (mapping to  $[-1, 1]$ ), and Sigmoid is used for vision outputs and absolute tactile predictions. During simulation pre-training, the network optimizes raw logits to avoid early saturation and maintain gradient flow.

Training is governed by a weighted multi-task objective:

$$\min \mathcal{L}_{\text{total}} = \lambda_t \mathcal{L}_t + \lambda_v \mathcal{L}_v, \quad (8)$$

where  $\lambda_t$  is the weight for the tactile loss  $\mathcal{L}_t$ , and  $\lambda_v$  is the weight for the vision loss  $\mathcal{L}_v$ .

In the first stage (simulation pre-training), we enforce pixel-accurate supervision:

$$\mathcal{L}_v = \mathcal{L}_{L1}, \quad (9)$$

$$\mathcal{L}_t = \mathcal{L}_{L1} + \lambda_{\text{grad}} \mathcal{L}_{\text{grad}}, \quad (10)$$

where  $\mathcal{L}_{L1}$  denotes the L1 distance between the predictions and ground truth, and  $\mathcal{L}_{\text{grad}}$  computes the L1 distance of the spatial gradients using Sobel-like kernels, forcing the network to sharpen the edges of physical indentations.

In the second stage (real-world fine-tuning), we introduce physics-based augmentation through random ambient offsets

and exposure scaling, and strengthen the loss with structural and perceptual terms:

$$\mathcal{L}_v = \mathcal{L}_{L1} + \lambda_{\text{perc}} \mathcal{L}_{\text{perc}}, \quad (11)$$

$$\mathcal{L}_t = \mathcal{L}_{L1} + \lambda_{\text{grad}} \mathcal{L}_{\text{grad}} + \lambda_{\text{SSIM}} \mathcal{L}_{\text{SSIM}} + \lambda_{\text{perc}} \mathcal{L}_{\text{perc}}, \quad (12)$$

where  $\mathcal{L}_{\text{SSIM}} = 1 - \text{SSIM}$ , with SSIM being the Structural Similarity Index Measure [35]. The perceptual loss  $\mathcal{L}_{\text{perc}}$  follows [36] and is computed using feature maps from predefined layers of a frozen VGG-16 network (relu1\_2, relu2\_2, relu3\_3) [37]. Both stages use AdamW [38] with a cosine-annealing learning-rate schedule [39] for optimization.

Recognizing the importance of structural integrity in physical contact representations, model selection is based on a weighted combination of SSIM and Learned Perceptual Image Patch Similarity (LPIPS) [40] across both modalities. The optimal model maximizes the overall score  $\mathcal{S}$ :

$$\mathcal{S} = \omega_{\text{ts}} \text{SSIM}_t - \omega_{\text{tl}} \text{LPIPS}_t + \omega_{\text{vs}} \text{SSIM}_v - \omega_{\text{vl}} \text{LPIPS}_v, \quad (13)$$

with weights  $\omega_{\text{ts}} = 1.0$ ,  $\omega_{\text{tl}} = 0.8$ ,  $\omega_{\text{vs}} = 0.5$ , and  $\omega_{\text{vl}} = 0.4$ . This configuration emphasize tactile quality while penalizing perceptual discrepancy, favoring models that recover fine contact geometries without degrading visual fidelity.

To isolate the effects of input context and residual learning, we evaluate three architectural variants: SI (Single-Input), DI-AbsT (Dual-Input, Absolute Tactile), and DI-ResT (Dual-Input, Residual Tactile). SI serves as the baseline, predicting the vision and tactile outputs solely from the current observation. DI-AbsT adds the non-contact reference image as an input, with the tactile decoder directly predicting the absolute tactile image (Option A in Fig. 4). DI-ResT represents our proposed configuration, which utilizes the reference image and predicts the visual output and a contact-induced tactile residual, which is added to the non-contact tactile background (Option B in Fig. 4). We exclude predicting a tactile residual from a single image without a non-contact reference, as the residual is not well-defined and tends to encourage memorization.

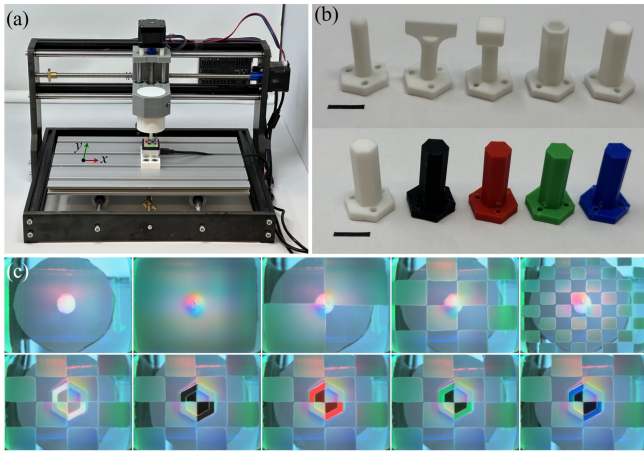


Fig. 5. Real-world data collection and dataset overview. (a) Automated 3-axis linear motion platform, where the  $x, y$ -axes align with the sensor contact plane for precise spatial sampling. (b) Indenter diversity. Top: five distinct geometries (sphere, edge, square, hollow octagon, solid octagon). Bottom: one geometry (hollow octagon) in five colors (white, black, red, green, blue) to improve visual robustness. Black scale bars correspond to 1 cm. (c) Representative data samples. Top: a white sphere indenter at 1.5 mm depth across five gel configurations. Bottom: a hollow octagon indenter in five colors captured with the  $4 \times 4$  patterned gel pad at 1.5 mm depth.

### III. REAL DATA COLLECTION AND MODEL ADAPTATION

To support the real-world fine-tuning of muxNet and reduce the sim-to-real gap, we built an automated tactile data acquisition system, as shown in Fig. 5 (a). The system uses a 3-axis linear motion platform driven by USB-serial G-code to execute repeatable indentations at fixed spatial coordinates.

We collect data with five indenter geometries (sphere, edge, square, solid octagon, hollow octagon) to cover different contact profiles. To promote generalization across visual appearances, each geometry was produced in five colors (white, black, red, green, and blue), resulting in 25 indenters (Fig. 5 (b)). For each indenter, we sample five locations on the sensor surface: the center  $(0, 0)$  and four peripheral points  $(0, -6.4)$ ,  $(0, 6.4)$ ,  $(5.2, 0)$ , and  $(-5.2, 0)$  mm, using the coordinate system in Fig. 5 (a). At each location, the indenter moves from a non-contact depth of 0 mm to 1.5 mm depth in 0.1 mm steps, capturing continuous gel deformation together with the associated visual occlusion.

We utilized five MuxGel configurations: a fully coated pad (pure tactile), a transparent pad (pure vision), and three multiplexed pads ( $2 \times 2$ ,  $4 \times 4$ , and  $8 \times 8$ ), with representative samples in Fig. 5 (c). Using an identical indentation protocol across pads ensures spatial and depth alignment across all samples. The tactile-only and vision-only pads therefore provide ground-truth targets for supervised fine-tuning of the multiplexed pads. For each multiplexed pad, we capture an initial non-contact reference image under dark conditions as the reference input for the DI-AbsT and DI-ResT variants. Separately, we capture a non-contact tactile background using the fully coated pad, which serves as the additive baseline for residual reconstruction.

This aligned real-world dataset supports the second training stage by adapting the shared encoder and task-specific

decoders to sensor-specific effects, including measurement noise, optical scattering, and gel dynamics. We split the dataset into 90% training and 10% validation sets and optimize the multi-task objective in Eq. (8) with physics-based augmentations. Model selection follows the score  $\mathcal{S}$  in Eq. (13), favoring models that preserve both contact-geometry fidelity and external visual reconstruction.

### IV. PERFORMANCE EVALUATION ON UNSEEN OBJECTS

To evaluate generalization, data is collected on nine unseen objects with diverse colors, textures, and geometric shapes (Fig. 6). Each object is mounted on the platform in Fig. 5 (a). Unlike the indenters used for real fine-tuning, the irregular shapes of these objects restrict the contact to a single central location. At this location, the platform indents the object from non-contact to 1.5 mm depth in 0.1 mm steps. Data are collected across the same five gel configurations.

We compare the three architectural variants (SI, DI-AbsT, DI-ResT) under two training settings (zero-shot simulation and real-data fine-tuning). For this evaluation, data from the three multiplexed configurations ( $2 \times 2$ ,  $4 \times 4$ , and  $8 \times 8$ ) are aggregated. The results are shown in Table I.

After fine-tuning, DI-ResT achieves the best overall tactile reconstruction performance. In particular, the tactile RMSE of the fine-tuned DI-ResT decreases to 0.0287, improving over the best zero-shot baseline (0.0830). This demonstrates accurate recovery of millimeter-scale real contact deformations. Furthermore, the results exhibit a classic trade-off between structure alignment and perceptual details. While the fine-tuned DI-AbsT and DI-ResT achieve nearly identical structure scores (tactile (1-SSIM): 0.0877 vs. 0.0878, a negligible difference), DI-ResT substantially improves perceptual quality, reducing tactile LPIPS from 0.1082 to 0.0489.

For vision, the zero-shot simulation model (DI-AbsT) attains a lower LPIPS (0.3119) than the fine-tuned models, but with markedly worse PSNR (17.79). This pattern suggests that the simulation-only model produces sharp but structurally inconsistent predictions, likely driven by simulated priors, which can yield favorable perceptual scores while failing to match the real scene. This behavior is also visible in Fig. 7. Real-world fine-tuning primarily addresses the larger domain gap in the tactile modality, leading to large gains in tactile metrics. The small increase in vision LPIPS reflects a secondary trade-off under joint multi-task optimization, while preserving the main objective of recovering accurate contact geometry and tactile deformation.

Next, we evaluated the reconstruction performance of the fine-tuned DI-ResT model across checkerboard configurations, as detailed in Table II. The results reveal a clear modality trade-off driven by the physical layout of the sensor.

For tactile reconstruction, the  $4 \times 4$  configuration achieves the best performance across metrics, suggesting that its block size provides an effective receptive-field scale for recovering localized contact deformation. Additionally, because the internal illumination of the sensor alters the object's appearance upon contact, the vision stream contains weak contact tactile cues during interaction. The  $4 \times 4$  pattern

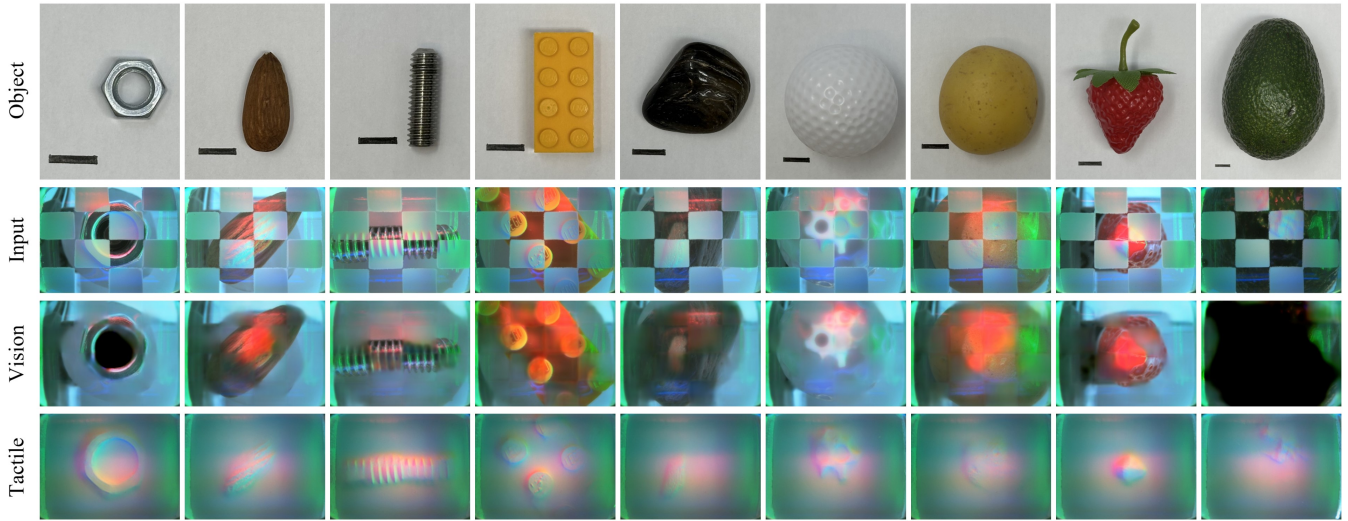


Fig. 6. Visuo-tactile reconstruction of real unseen objects using the DI-ResT after real-world fine-tuning. Row 1: Nine test objects (screw nut, almond, stub, LEGO block, stone, plastic golf ball, potato, plastic strawberry, avocado) used to test model generalization. Black scale bars correspond to 1 cm. Row 2: Raw multiplexed inputs from the 4x4 checkerboard configuration. Row 3: Reconstructed vision outputs recovering occluded region. Row 4: Reconstructed tactile outputs recovering localized high-frequency contact deformation.

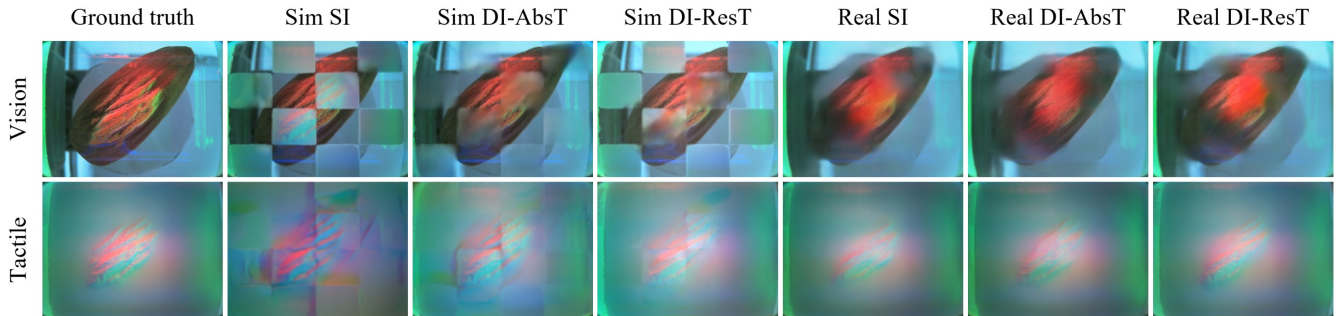


Fig. 7. Qualitative reconstruction results on the almond object. Top: vision; bottom: tactile. Left to right: Ground Truth; zero-shot simulation (Sim) models (SI, DI-AbsT, DI-ResT); and real-data fine-tuned models (SI, DI-AbsT, DI-ResT).

TABLE I  
QUANTITATIVE EVALUATION OF THE MODELS ON REAL UNSEEN OBJECTS.

Training Stage	Architecture	Tactile Reconstruction				Vision Reconstruction			
		RMSE ↓	(1-SSIM) ↓	LPIPS ↓	PSNR ↑	RMSE ↓	(1-SSIM) ↓	LPIPS ↓	PSNR ↑
Simulation (Zero-shot)	SI	0.0929	0.1667	0.3749	20.6384	0.2198	0.3651	0.3900	13.1892
	DI-AbsT	0.1260	0.1697	0.2025	18.0412	0.1294	0.3182	<b>0.3119</b>	17.7973
	DI-ResT	0.0830	0.1227	0.1094	21.6298	0.1553	0.3319	0.3398	16.2726
Real (Fine-tuned)	SI	0.0332	0.0956	0.0977	29.5972	<b>0.1030</b>	0.2822	0.3557	<b>19.7613</b>
	DI-AbsT	0.0770	<b>0.0877</b>	0.1082	24.6348	0.1118	<b>0.2799</b>	0.3339	19.1292
	<b>DI-ResT</b>	<b>0.0287</b>	0.0878	<b>0.0489</b>	<b>31.0549</b>	0.1058	0.3098	0.3232	19.5489

Note: Best results in **bold**. The vision decoder consistently predicts absolute images. SI: Single-Input, DI: Dual-Input, AbsT: Absolute Tactile, ResT: Residual Tactile. Structural similarity index measure is reported as (1-SSIM).

provides a balanced ratio of coated (tactile) and transparent (vision) regions, avoiding a severe tactile bottleneck while still allowing cross-modal information to be exploited.

Conversely, for vision reconstruction, the  $8 \times 8$  configuration yields the best performance. As vision depends on global context, smaller and more densely distributed occluded regions minimize the spatial gaps in visual content, which simplifies interpolation for the network.

Due to the inherent nature of visuo-tactile fusion, where tactile sensing prioritizes local high-frequency deformation details, while vision prioritizes global structural context, the hardware configuration inevitably presents a trade-off. Considering that robotic manipulation tasks typically rely on high-fidelity, localized contact data to ensure stability, the  $4 \times 4$  configuration was selected as the optimal hardware setup for the subsequent manipulation experiments.

TABLE II  
 QUANTITATIVE EVALUATION OF THE PROPOSED FINE-TUNED DI-RES<sub>T</sub> ARCHITECTURE AFTER REAL FINE-TUNING UNDER DIFFERENT CONFIGURATIONS ON REAL UNSEEN OBJECTS.

Configuration	Tactile Reconstruction				Vision Reconstruction			
	RMSE ↓	(1-SSIM) ↓	LPIPS ↓	PSNR ↑	RMSE ↓	(1-SSIM) ↓	LPIPS ↓	PSNR ↑
2 × 2	0.0301	0.0879	0.0484	30.6372	0.1185	0.3132	0.3457	18.5543
4 × 4	<b>0.0285</b>	<b>0.0869</b>	<b>0.0481</b>	<b>31.2080</b>	0.1021	0.3053	0.3136	19.8327
8 × 8	0.0290	0.0891	0.0513	31.0296	<b>0.0935</b>	<b>0.3015</b>	<b>0.3059</b>	<b>20.5986</b>

Note: Best results among the individual configurations are highlighted in **bold**. All models utilize the Fine-tuned DI-Res<sub>T</sub> architecture. Structural similarity index measure is reported as (1-SSIM).

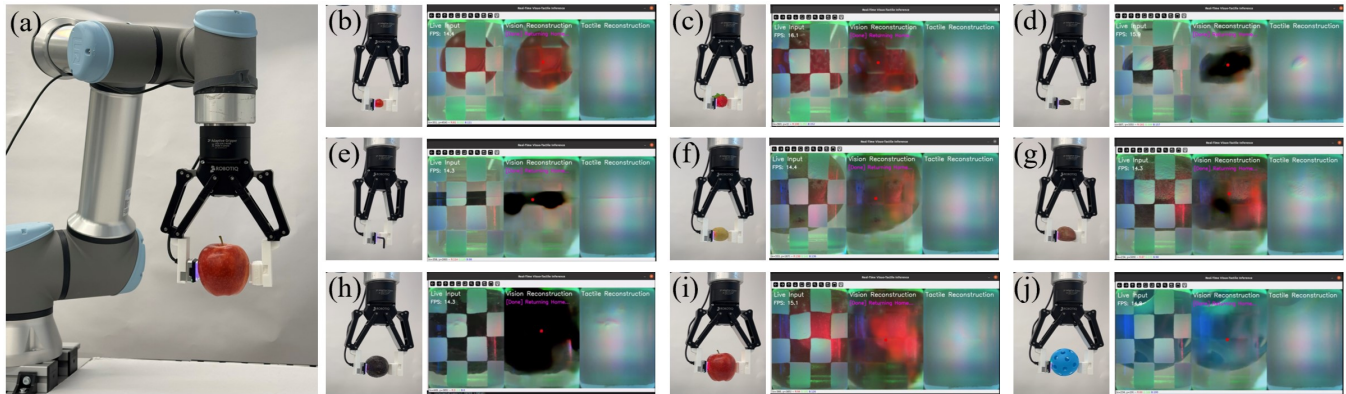


Fig. 8. Visuo-tactile servoing grasping experiment. (a) Experimental setup featuring the proposed sensor integrated with a Robotiq gripper. (b-j) Successful grasp executions across a diverse set of unseen objects. For each object, the left panel depicts the stable physical grasp, while the right panel displays the real-time system interface: capturing the raw sensor input, the reconstructed vision output with contour-center tracking for alignment, and the reconstructed GelSight-style tactile image upon contact. The tested objects include: (b) cherry tomato, (c) plastic strawberry, (d) stone, (e) hex key, (f) potato, (g) red potato, (h) avocado, (i) apple, and (j) pickleball.

## V. VISUAL-TACTILE SERVOING GRASPING EXPERIMENT

To evaluate the sensor in a manipulation setting, we designed a dynamic visuo-tactile servoing experiment for robotic grasping. MuxGel was integrated into a Robotiq 2F-140 gripper mounted on a UR16e robotic arm. The robot was constrained to vertical translation (Z-axis) directly above the target objects initially. During the approach phase, the arm descends until the object appears in the sensor’s visual field of view. Object localization is achieved via background subtraction and contour extraction. A visual servoing loop continuously computes the object centroid and drives the arm to minimize its vertical offset relative to the sensor center. After alignment, the gripper initiates a gentle closure.

During closure, the Robotiq 2F-140 jaws do not follow a perfectly parallel, purely normal trajectory, which can induce in-plane object shift. We track this motion online using the vision stream and compensate in real time to maintain grasp alignment. The controller then switches to tactile stopping based on reconstructed contact deformation. The gripper stops closing when the maximum deformation in the reconstructed tactile depth map exceeds a predefined threshold. This stopping rule aims to achieve stable contact while avoiding excessive compression before lifting. Notably, 3D tactile depth reconstruction (shown in the supplementary video) is performed zero-shot using the standard GelSight

Mini repository [41] without any domain adaptation. This demonstrates that the reconstructed tactile outputs maintain high physical fidelity and are fully compatible with existing tactile processing pipelines. The proposed pipeline was evaluated across nine unseen objects, achieving a 100% successful grasp rate.

## VI. CONCLUSION

In this paper, we present MuxGel, a novel spatially multiplexed design that enables simultaneous dual-modal visuo-tactile sensing in vision-based tactile sensors. By using a checkerboard coating with a deep reconstruction model, MuxGel effectively decouples and restores visual and tactile signals from the same camera stream. Experiments show accurate reconstruction and strong generalization to unseen objects. Crucially, MuxGel preserves the pad geometry and mechanical interface of GelSight, enabling plug-and-play integration by replacing only the gel pad, without optical or mechanical changes. Validation within the GelSight platform further confirms its compatibility and ease of deployment.

While this work targets the GelSight format, the spatial multiplexing principle is sensor-agnostic and can be extended to other fully coated vision-based tactile sensors. Future research will focus on optimizing the reconstruction algorithms to handle more complex environmental lighting.

Furthermore, we intend to systematically investigate multi-plexing designs that vary pattern geometry and the visuo-tactile area ratio to quantify trade-offs in reconstruction and manipulation. We also plan to use the dual-modality signal for downstream tasks such as visuo-tactile pose estimation and closed-loop manipulation in less controlled settings.

## REFERENCES

- [1] J. Cui and J. Trinkle, "Toward next-generation learned robot manipulation," *Science robotics*, vol. 6, no. 54, p. eabd9461, 2021.
- [2] Q. K. Luu, P. Zhou, Z. Xu, Z. Zhang, Q. Qiu, and Y. She, "Manifeel: Benchmarking and understanding visuotactile manipulation policy learning," *arXiv preprint arXiv:2505.18472*, 2025.
- [3] Z. Xu, R. Uppuluri, X. Zhang, C. Fitch, P. G. Crandall, W. Shou, D. Wang, and Y. She, "Unit: Data efficient tactile representation with generalization to unseen objects," *IEEE Robotics and Automation Letters*, 2025.
- [4] M. R. I. Prince, S. Athar, P. Zhou, and Y. She, "Tacsopce: A miniaturized vision-based tactile sensor for surgical applications," *Advanced Robotics Research*, p. e202500117, 2025.
- [5] W. Lin, Z. Wang, Y. Xu, Z. Hu, W. Zhao, Z. Zhu, Z. Sun, G. Wang, and Z. Peng, "Self-adaptive perception of object's deformability with multiple deformation attributes utilizing biomimetic mechanoreceptors," *Advanced Materials*, vol. 36, no. 9, p. 2305032, 2024.
- [6] Y. Zhou, P. Zhou, S. Wang, and Y. She, "In-hand singulation, scooping, and cable untangling with a 5-dof tactile-reactive gripper," *Advanced Robotics Research*, vol. 1, no. 2, p. 202500020, 2025.
- [7] Y. Gao, S. Matsuoka, W. Wan, T. Kiyokawa, K. Koyama, and K. Harada, "In-hand pose estimation using hand-mounted rgb cameras and visuotactile sensors," *IEEE Access*, vol. 11, pp. 17218–17232, 2023.
- [8] Z. Zhang, Z. Xu, J. N. Lakamsani, and Y. She, "Canonical policy: Learning canonical 3d representation for se (3)-equivariant policy," *arXiv preprint arXiv:2505.18474*, 2025.
- [9] Z. Hu, L. Lin, W. Lin, Y. Xu, X. Xia, Z. Peng, Z. Sun, and Z. Wang, "Machine learning for tactile perception: advancements, challenges, and opportunities," *Advanced Intelligent Systems*, vol. 5, no. 7, p. 2200371, 2023.
- [10] W. Yuan, S. Dong, and E. H. Adelson, "Gelsight: High-resolution robot tactile sensors for estimating geometry and force," *Sensors*, vol. 17, no. 12, p. 2762, 2017.
- [11] B. Ward-Cherrier, N. Pestell, L. Cramphorn, B. Winstone, M. E. Giannaccini, J. Rossiter, and N. F. Lepora, "The tactip family: Soft optical tactile sensors with 3d-printed biomimetic morphologies," *Soft robotics*, vol. 5, no. 2, pp. 216–227, 2018.
- [12] G. Zhang, Y. Du, H. Yu, and M. Y. Wang, "Deltact: A vision-based tactile sensor using a dense color pattern," *IEEE Robotics and Automation Letters*, vol. 7, no. 4, pp. 10778–10785, 2022.
- [13] C. Lin, Z. Lin, S. Wang, and H. Xu, "Dtact: A vision-based tactile sensor that measures high-resolution 3d geometry directly from darkness," in *2023 IEEE International Conference on Robotics and Automation (ICRA)*. IEEE, 2023, pp. 10359–10366.
- [14] A. N. Chaudhury, T. Man, W. Yuan, and C. G. Atkeson, "Using collocated vision and tactile sensors for visual servoing and localization," *IEEE Robotics and Automation Letters*, vol. 7, no. 2, pp. 3427–3434, 2022.
- [15] K. Shimonomura, H. Nakashima, and K. Nozu, "Robotic grasp control with high-resolution combined tactile and proximity sensing," in *2016 IEEE International Conference on Robotics and automation (ICRA)*. IEEE, 2016, pp. 138–143.
- [16] D. Zhang, W. Fan, J. Lin, H. Li, Q. Cong, W. Liu, N. F. Lepora, and S. Luo, "Design and benchmarking of a multimodality sensor for robotic manipulation with gan-based cross-modality interpretation," *IEEE Transactions on Robotics*, vol. 41, pp. 1278–1295, 2025.
- [17] W. Fan, H. Li, W. Si, S. Luo, N. Lepora, and D. Zhang, "Vitatip: Design and verification of a novel biomimetic physical vision-tactile fusion sensor," in *2024 IEEE International Conference on Robotics and Automation (ICRA)*. IEEE, 2024, pp. 1056–1062.
- [18] Q. Wang, Y. Du, and M. Y. Wang, "Spectac: A visual-tactile dual-modality sensor using uv illumination," in *2022 international conference on robotics and automation (ICRA)*. IEEE, 2022, pp. 10844–10850.
- [19] A. Yamaguchi and C. G. Atkeson, "Tactile behaviors with the vision-based tactile sensor fingervision," *International Journal of Humanoid Robotics*, vol. 16, no. 03, p. 1940002, 2019.
- [20] Y. Dong, J. Ren, Z. Liu, Z. Peng, Z. Yuan, N. Zhang, and G. Gu, "Look-to-touch: a vision-enhanced proximity and tactile sensor for distance and geometry perception in robotic manipulation," *IEEE/ASME Transactions on Mechatronics*, 2026.
- [21] S. Athar, G. Patel, Z. Xu, Q. Qiu, and Y. She, "Vistac toward a unified multimodal sensing finger for robotic manipulation," *IEEE Sensors Journal*, vol. 23, no. 20, pp. 25440–25450, 2023.
- [22] Q. K. Luu, D. Q. Nguyen, N. H. Nguyen, and V. A. Ho, "Soft robotic link with controllable transparency for vision-based tactile and proximity sensing," in *2023 IEEE international conference on soft robotics (roboSoft)*. IEEE, 2023, pp. 1–6.
- [23] N. H. Nguyen, N. M. D. Le, Q. K. Luu, T. T. Nguyen, and V. A. Ho, "Vi2tap: A cross-polarization based mechanism for perception transition in tactile-proximity sensing with applications to soft grippers," *IEEE Robotics and Automation Letters*, 2025.
- [24] F. R. Hogan, J.-F. Tremblay, B. H. Baghi, M. Jenkin, K. Siddiqi, and G. Dudek, "Finger-sts: Combined proximity and tactile sensing for robotic manipulation," *IEEE Robotics and Automation Letters*, vol. 7, no. 4, pp. 10865–10872, 2022.
- [25] P. Isola, J.-Y. Zhu, T. Zhou, and A. A. Efros, "Image-to-image translation with conditional adversarial networks," in *Proceedings of the IEEE conference on computer vision and pattern recognition*, 2017, pp. 1125–1134.
- [26] G. Liu, F. A. Reda, K. J. Shih, T.-C. Wang, A. Tao, and B. Catanzaro, "Image inpainting for irregular holes using partial convolutions," in *Proceedings of the European conference on computer vision (ECCV)*, 2018, pp. 85–100.
- [27] X. Zhang, R. Ng, and Q. Chen, "Single image reflection separation with perceptual losses," in *Proceedings of the IEEE conference on computer vision and pattern recognition*, 2018, pp. 4786–4794.
- [28] K. He, X. Zhang, S. Ren, and J. Sun, "Deep residual learning for image recognition," in *Proceedings of the IEEE conference on computer vision and pattern recognition*, 2016, pp. 770–778.
- [29] O. Ronneberger, P. Fischer, and T. Brox, "U-net: Convolutional networks for biomedical image segmentation," in *International Conference on Medical image computing and computer-assisted intervention*. Springer, 2015, pp. 234–241.
- [30] L. Downs, A. Francis, N. Koenig, B. Kinman, R. Hickman, K. Reymann, T. B. McHugh, and V. Vanhoucke, "Google scanned objects: A high-quality dataset of 3d scanned household items," in *2022 International Conference on Robotics and Automation (ICRA)*. IEEE, 2022, pp. 2553–2560.
- [31] E. Todorov, T. Erez, and Y. Tassa, "Mujoco: A physics engine for model-based control," in *2012 IEEE/RSJ International Conference on Intelligent Robots and Systems*. IEEE, 2012, pp. 5026–5033.
- [32] K. Zakka, "Scanned Objects MuJoCo Models," 7 2022. [Online]. Available: [https://github.com/kevinzakka/mujoco-scanned\\_objects](https://github.com/kevinzakka/mujoco-scanned_objects)
- [33] Z. Si and W. Yuan, "Taxim: An example-based simulation model for gelsight tactile sensors," *IEEE Robotics and Automation Letters*, vol. 7, no. 2, pp. 2361–2368, 2022.
- [34] A. Quattoni and A. Torralba, "Recognizing indoor scenes," in *2009 IEEE conference on computer vision and pattern recognition*. IEEE, 2009, pp. 413–420.
- [35] Z. Wang, A. C. Bovik, H. R. Sheikh, and E. P. Simoncelli, "Image quality assessment: from error visibility to structural similarity," *IEEE transactions on image processing*, vol. 13, no. 4, pp. 600–612, 2004.
- [36] J. Johnson, A. Alahi, and L. Fei-Fei, "Perceptual losses for real-time style transfer and super-resolution," in *European conference on computer vision*. Springer, 2016, pp. 694–711.
- [37] K. Simonyan and A. Zisserman, "Very deep convolutional networks for large-scale image recognition," *arXiv preprint arXiv:1409.1556*, 2014.
- [38] I. Loshchilov and F. Hutter, "Decoupled weight decay regularization," *arXiv preprint arXiv:1711.05101*, 2017.
- [39] —, "SGDR: Stochastic gradient descent with warm restarts," in *International Conference on Learning Representations*, 2017.
- [40] R. Zhang, P. Isola, A. A. Efros, E. Shechtman, and O. Wang, "The unreasonable effectiveness of deep features as a perceptual metric," in *Proceedings of the IEEE conference on computer vision and pattern recognition*, 2018, pp. 586–595.
- [41] GelSight, Inc., "Gelsight robotics software," accessed: 2026-03-01. [Online]. Available: <https://github.com/gelsightinc/gsrobotics>